Chapter 2

Experimental approaches and techniques

2.1. Pre-synthesis protocols and setups

2.1.1. Preparation of doubly distilled water

Doubly distilled (DD) water was prepared using a two sequential single-stage glass distillation unit (Borosilicate DD water production setup) to ensure high purity and removal of ionic and organic contaminants. This ultrapure DD water was used throughout all synthesis procedures to maintain the consistency and reliability of the experimental results. The use of DD water minimizes the risk of introducing extraneous impurities that could potentially affect reaction mechanisms. The use of DD water was particularly critical in processes involving sensitive reagents, precise pH adjustments, and the synthesis of pristine and nanocomposite materials. All necessary precautionary measures were strictly followed during the preparation and storage of the DD water to prevent any form of contamination.

2.1.2. Glassware handling protocols

Clean, impurity-free glassware is essential, particularly when synthesizing nanomaterials, to ensure experimental accuracy. All glassware, including beakers, round-bottom flasks, and measuring cylinders, was thoroughly cleaned with high-grade dishwasher gel to remove visible residues and contaminants. This was followed by rinsing with propanol to eliminate any remaining organic impurities and to facilitate rapid drying due to its volatile nature. For glassware intended for use with DD water as a solvent, an additional rinse with distilled water was performed to ensure complete removal of residual propanol. After rinsing, the glassware was dried in a laboratory oven at an appropriate temperature (typically 60-80 ºC) to remove any traces of moisture or solvent. This protocol ensured that volumetric measurements remained accurate and that the integrity of the synthesis process was maintained by avoiding contamination from residual solvents or moisture. To enable reuse, glassware was rinsed immediately after use to prevent residues from hardening. For organic and inorganic contaminants, it was first cleaned with acetone or ethanol, followed by soaking in a dilute acid or base solution to neutralize any remaining residues. The glassware was then thoroughly rinsed with distilled water to ensure complete removal

of solvents and cleaning agents. Prior to reuse, each item was carefully inspected for cracks or stress marks, and damaged glassware was discarded according to laboratory safety guidelines.

2.2. Synthesis procedures

The following synthesis methods were employed to prepare the photocatalytic samples. An overview of the general procedure, along with the specific steps involved, are discussed in the sections below.

2.2.1. Sol-gel method

This method, as illustrated in Figure 2.1, was used to synthesize metal oxide photocatalysts at room temperature. Initially, metal precursors such as alkoxides or salts are dissolved in a solvent, typically alcohol or water. The precursor undergoes hydrolysis followed by polycondensation, resulting in the formation of a colloidal sol. As the reaction progresses, the sol transforms into a gel with a porous network. The gel is then aged to strengthen the structure and subsequently dried to obtain the sample.

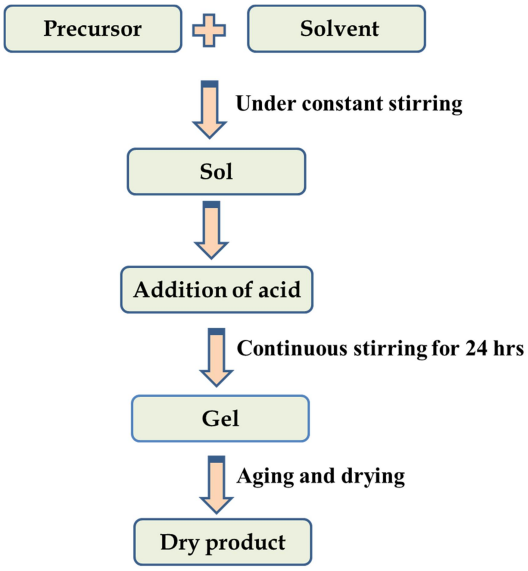

Figure 2.1. Illustration of sol-gel method.

2.2.2. Modified sol-gel method

This method was employed to synthesize doped metal oxide photocatalysts or composites integrated with co-catalysts at room temperature. Figure 2.2 shows a block diagram illustrating the step-by-step synthesis procedure. Metal precursors were

sequentially added to the solvent prior to sol formation to obtain the desired composite. However, for metal sensitization on the composite, metal particles were first dispersed in a suitable medium before being introduced into the sol, after which the standard sol-gel process was followed.

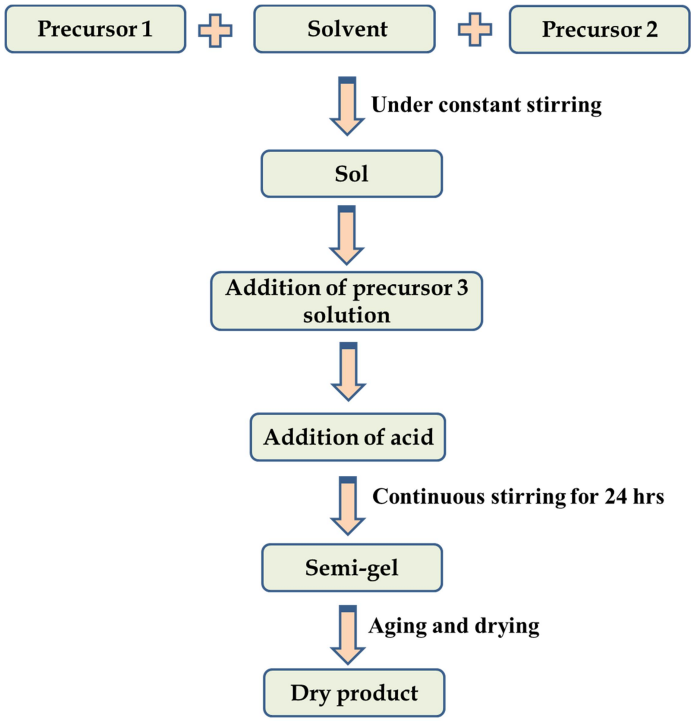

Figure 2.2. Illustration of modified sol-gel method.

2.2.3. Co-precipitation method

This method was used to synthesize metal hydroxide and chromate materials at a controlled temperature. The block diagram, as shown in Figure 2.3, demonstrates the synthesis procedure step by step. Metal salts (e.g., nitrates, sulfates, or chlorides) containing the desired cations and counterions are dissolved in a solvent, typically water. A precipitating agent (e.g., NaOH or Na_2CO_3) is then added to adjust the pH, leading to the formation of insoluble hydroxides or carbonates. The resulting precipitate aggregates and grows into a solid phase, which is subsequently centrifuged, thoroughly washed, and dried. Finally, the dried material is heat-treated to obtain the desired crystalline structure.

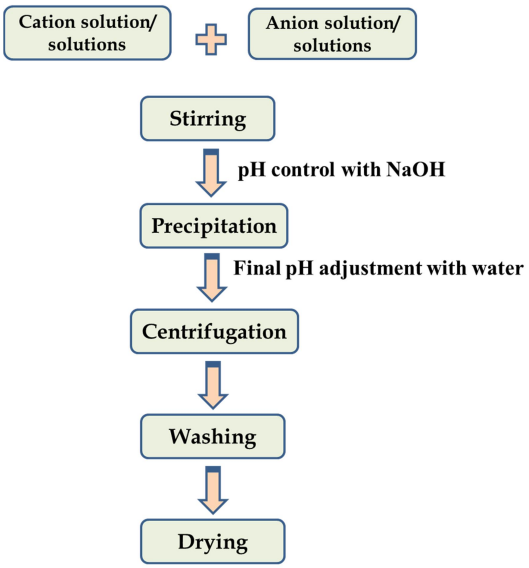

Figure 2.3. Illustration of co-precipitation method.

2.2.4. Reduction method

This method was used to synthesize metal nanoparticles at room temperature. In a typical synthesis, a solution of the metal precursor is prepared, followed by the addition of a capping and stabilizing agent in a suitable solvent under constant stirring. An etching agent was then introduced with continued stirring, and finally, the mixture was reduced using a reducing agent to yield either a metal nanoparticle dispersion or a metal precipitate. A block diagram of the method is shown in Figure 2.4.

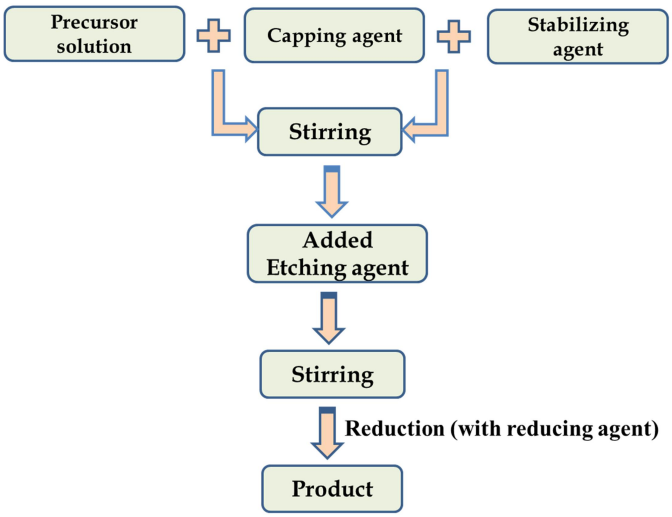

Figure 2.4. Illustration of reduction method.

2.3. Post-synthesis methods

2.3.1. Centrifugation

After synthesis, the precipitate was separated from the solvent by centrifugation at 8000-10000 RPM for 5-10 minutes, depending on the requirement. The solid precipitate settled at the bottom and was separated from the supernatant by carefully removing the latter with a micropipette. Figure 2.5 illustrates the procedure by which supernatant and sample precipitate is obtained after centrifugation.

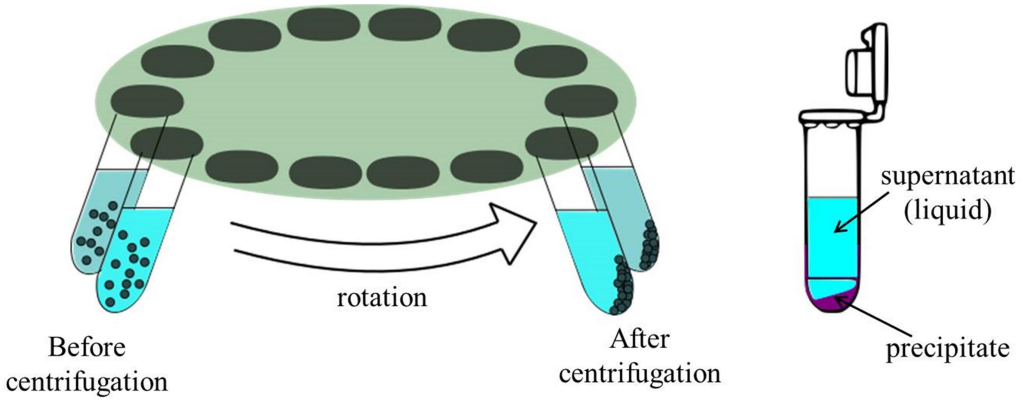

Figure 2.5. Illustration of centrifugation process. The solid sample particles are forced down to accumulate at the bottom of centrifuge tube by centrifugal force, after which the unwanted liquid is removed using a micropipette.

2.3.2. Calcination

The powdered samples were calcined in muffle furnaces, including chamber and tube furnaces, as shown in Figure 2.6. The different temperatures at which samples were calcined ranged from 400 to 700 ºC. The ramping rate was set at 10 ºC per min wherever applicable. All the samples were calcined for 2 hours.

2.3.3. Grinding

The air-dried samples or vacuum dried solid samples were ground into fine powder using a mortar-pestle, as shown in Figure 2.7. The powdered samples were then collected with a spatula and stored in air-sealed tubes for further use, characterization and applications.

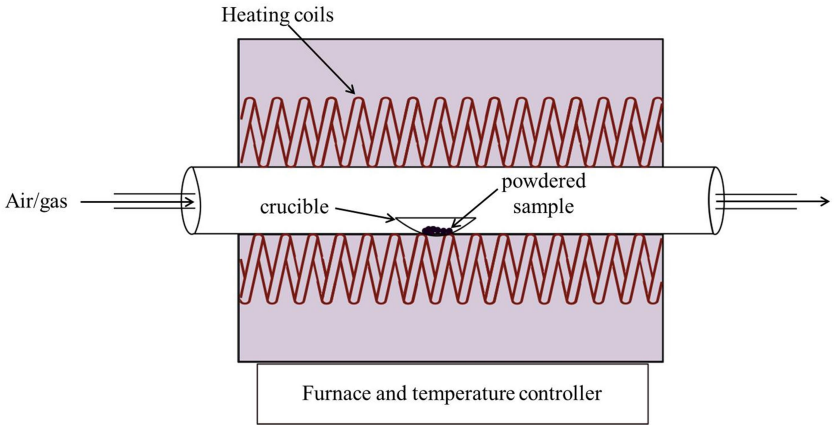

Figure 2.6. Schematic diagram of the tube furnace with the sample placed inside.

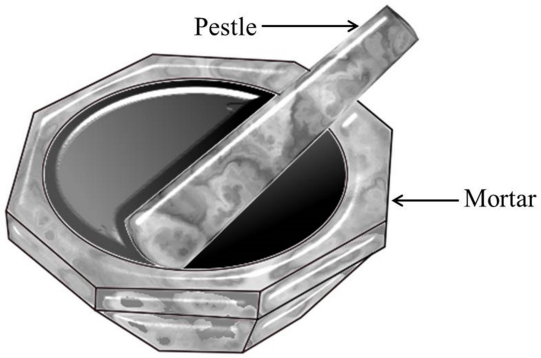

Figure 2.7. Mortar and pestle.

2.3.4. Drying

The wet solid samples obtained after centrifugation were first air-dried at room temperature to remove surface moisture. They were then vacuum-dried in a laboratory oven and stored in a desiccator to eliminate any remaining traces of solvent. This multi-step drying process ensured that the samples were completely free of residual water, which is essential to prevent agglomeration and preserve the desired morphology of nanomaterials.

2.3.5. Ultrasonication

The obtained powder samples were washed by dispersing them in a suitable solvent, such as distilled water or propanol, followed by sonication in an ultrasonicator bath. The mixture was later centrifuged to recover the sample precipitate. This process was

repeated for three-four cycles. Figure 2.8 illustrates the sample under sonication in ultrasonicator bath.

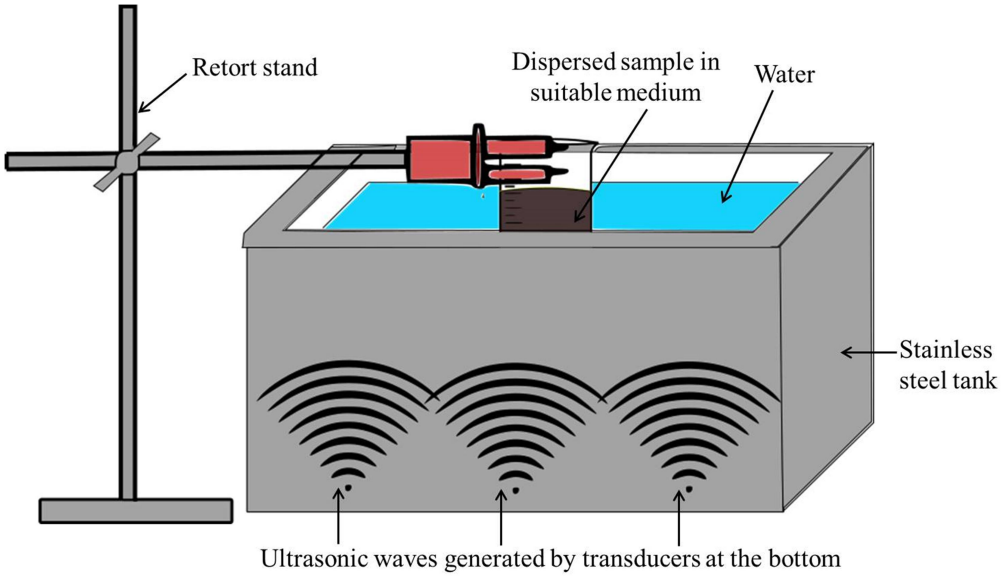

Figure 2.8. Illustration of ultrasonication. A sample in a suitable solvent is placed in a ultrasonicator bath.

2.4. Characterization

The following characterizations were performed to determine the structure-morphological properties of the photocatalytic materials

2.4.1. X-ray diffraction

The X-ray diffraction (XRD) patterns of the powdered photocatalysts were obtained using X-ray diffractometer system (Bruker-D8-AXS Advance XRD, Bruker D8 ADVANCE ECO P-XRD) equipped with Cu Kα X-ray source emitting radiation at λ = 1.54 Å. Bragg's law describes the condition for constructive interference of X-rays scattered by a crystalline material:

$$n\lambda = 2dsin\theta \quad (2.1)$$

where n is an integer representing the order of diffraction, λ is the wavelength of the incident X-rays, d is the interplanar spacing between crystal planes, and θ is the angle of incidence, illustrated in Figure 2.9.

The XRD spectra of samples were compared with reference files from the JCPDS database to identify the material. The peak positions were carefully matched to determine the phase, crystal symmetry, and lattice planes. The largest crystallite size (D) was determined from the most intense peak in the spectrum using Debye-Scherrer equation:

$$D = \frac{k\lambda}{\beta cos\theta} \tag{2.2}$$

where k is shape factor constant, which ranges from 0.62 to 2.08, λ denotes the X-ray wavelength, β denotes the full width (in radians) at half maxima (FWHM) of the diffraction peak, θ is the angle of diffraction.

The average crystallite size was obtained by taking the mean of the crystallite size calculated for all the peaks present in the spectra. The average crystallite size (D) was also calculated using Williamson-Hall plot between $\beta cos\theta$ vs $sin\theta$ governed by equation:

$$\beta cos\theta = 4\varepsilon\, sin\theta + \frac{k\lambda}{D} \tag{2.3}$$

where the slope and the y-intercept gives the value of strain (ε) and crystallite size (D), respectively. Here, β denotes the full width (in radians) at half maxima (FWHM) of the diffraction peak, θ is the angle of diffraction, k is shape factor constant, which ranges from 0.62 to 2.08.

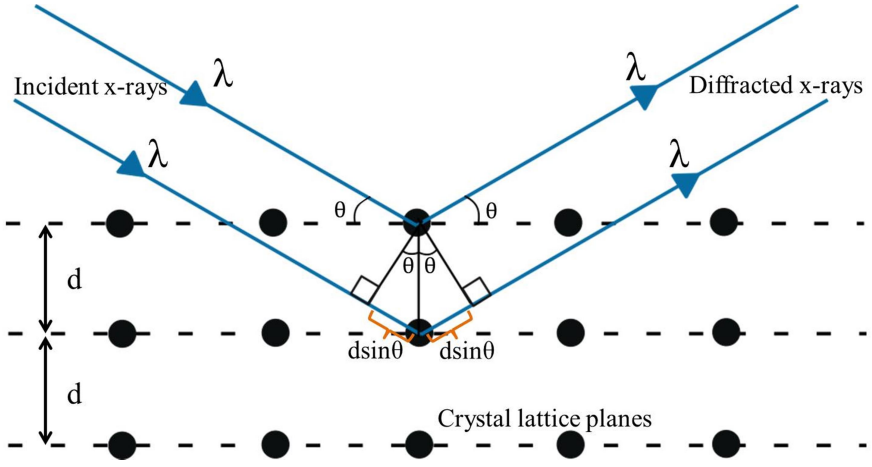

Figure 2.9. Bragg's law of X-ray diffraction.

2.4.2. Raman spectroscopy

Raman spectroscopy plays a crucial role in the characterization of nanomaterials, offering deep insight into their structural, vibrational, and chemical properties. It is particularly valuable for identifying phase compositions of heterojunction or polymorphs of a system. Raman spectroscopy operates on the principle of inelastic light scattering, in which incident monochromatic light interacts with molecular vibrations in a sample. For this technique, a laser source of wavelength 514 nm laser in the Renishaw Basis Series Raman spectrometer was used. While most of the light is scattered elastically (known as Rayleigh scattering), a small fraction is scattered inelastically. This results in an energy shift in the scattered photons that corresponds to the vibrational energy levels of the molecules. This energy shift provides a unique spectral fingerprint, revealing information about the molecular structure, bonding, and crystallinity of the material. Different polymorphs of metal oxides exhibited distinct Raman spectra, enabling the identification of M-O (metal-oxygen) stretching modes. Peak shifts and broadening provided insights into nanoscale effects due to phonon confinement. Additionally, Raman shifts indicated the presence of adsorbed species, such as OH^-, CO_2, and dopants on the oxide surface.

2.4.3. Scanning electron microscopy

Scanning electron microscopy (SEM) and Field-emission SEM was performed using a Hitachi S4200 and SIGMA VP FESEM (ZEISS) to investigate the morphological characteristics of the prepared samples. Particle size was measured from the images, and structural formation was analyzed at various magnifications. The working principle of SEM instrument is illustrated in Figure 2.10.

2.4.4. Transmission electron microscopy

Transmission electron microscopy (TEM) was conducted using an FEI Tecnai G2 F20, JEM-100 CX II, and JEM-2100 PLUS (HR) (JEOL) to analyze the structural and morphological features of the material. The working principle of TEM instrument is illustrated in Figure 2.11. High-resolution TEM (HRTEM) images were used to determine and identify the interplanar spacings of crystal planes in the aid of imaging software ‘ImageJ’. Selected area electron diffraction (SAED) patterns further facilitated interplanar spacing calculations as illustrated in Figure 2.12. Additionally, energy-

dispersive X-ray spectroscopy (EDX) was performed in tandem to determine the elemental composition of the photocatalyst.

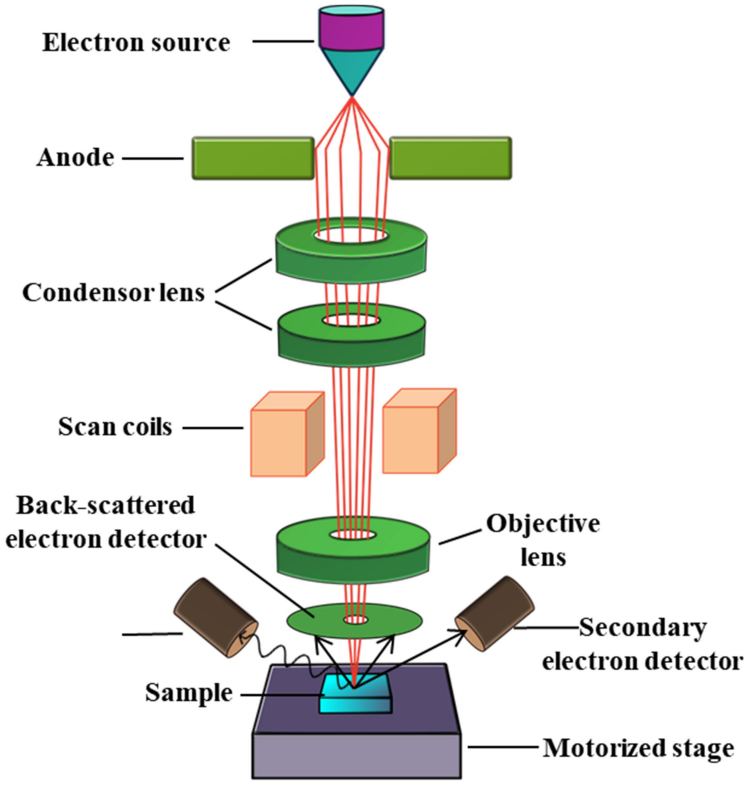

Figure 2.10. Schematic diagram of SEM.

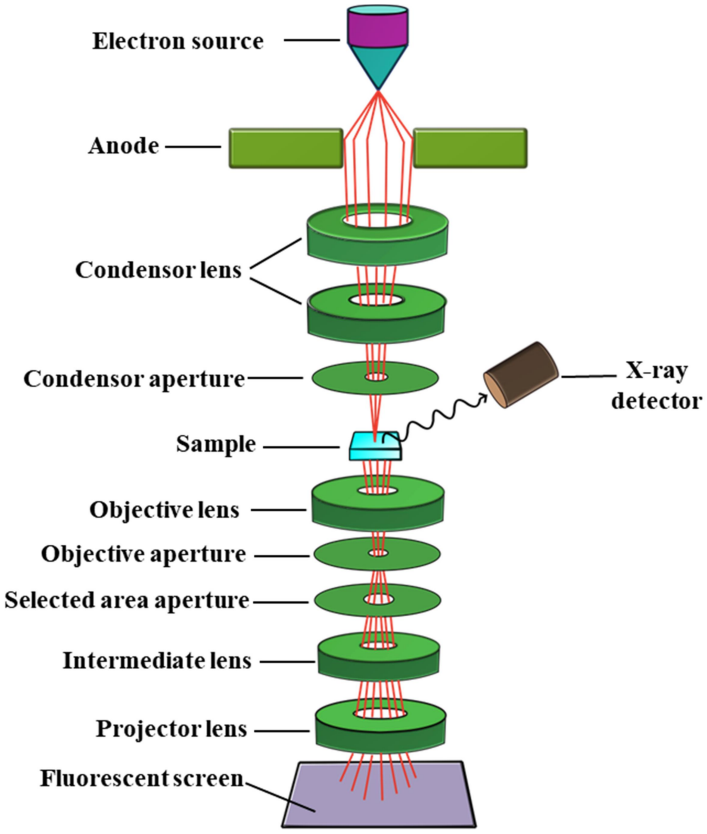

Figure 2.11. Schematic diagram of TEM.

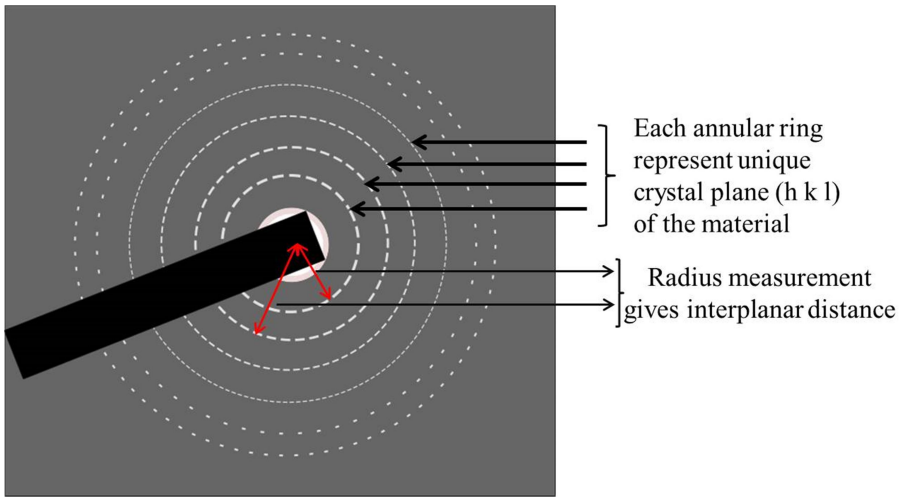

Figure 2.12. Illustration of SAED pattern.

The following characterizations were done to determine the optical properties of the photocatalytic materials:

2.4.5. Photoluminescence and time-resolved photoluminescence

The photoluminescence (PL) spectra and time-resolved PL spectra were recorded using a photoluminescence spectrophotometer (FluoroMax-4C; 1379D, UK) and a pico-second lifetime spectrophotometer (Lifespec II, Edinberg Instruments), respectively.

The emission peaks in the PL spectrum correspond to electronic transitions, providing insights into the bandgap energy of the semiconductor and enabling distinction between direct and indirect bandgap transitions. The PL intensity and decay behaviour offer valuable information on electron-hole recombination mechanisms, where strong PL signals indicate high recombination rates, while weak signals suggest efficient charge separation. Additionally, PL spectra can reveal changes in the electronic structure induced by doping with elements such as rare earth or transition metals, with shifts in emission peaks indicating modifications in defect states or band structure. Figure 2.13 shows various transitions possible in metal oxides that can lead to emission of luminescence photon.

Time-resolved photoluminescence (TRPL) enables the study of charge carrier behavior by tracking the temporal evolution of photoluminescence signals. The resulting decay curves reflect various recombination processes, including rapid radiative recombination and slower non-radiative events such as trap-mediated recombination. To analyze these decays, multi-exponential fitting is applied, providing discrete time constants that correspond to specific phenomena like bulk recombination, surface defect recombination, or interfacial charge transfer in composite materials. These time constants offer insights into electron–hole recombination dynamics, the efficiency of charge separation, and the influence of defects or traps on carrier mobility. Additionally, TRPL helps elucidate carrier migration pathways and their lifetimes, which is critical for understanding the performance of photocatalytic and optoelectronic systems.

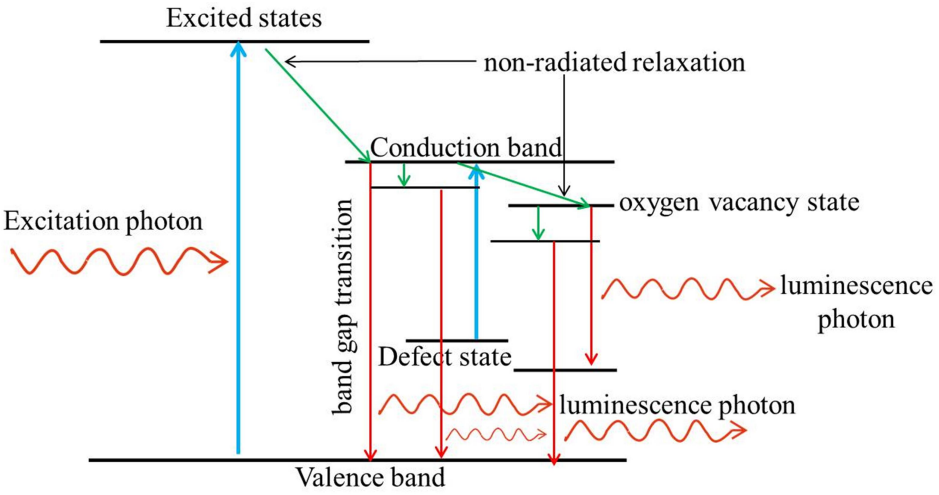

Figure 2.13. Energy diagram showing various transitions that produces photoluminescence.

2.4.6. UV-visible-diffuse reflectance spectrometer

The optical absorption properties of the solid samples were analyzed using a Ultraviolet-visible-Diffuse Reflectance Spectrometer (UV-vis-DRS), make: Shimadzu model: UV-1800. The absorption spectra was obtained from diffuse reflectance data R % using the following formula

$$\text{Absorbance} = -\log(R) \tag{2.4}$$

The spectra provided insights into the material's optical activity, indicating whether it is responsive to visible or UV light. Additionally, the absorption data was utilized in Tauc plot analysis to determine the material's bandgap energy as follows.

The Kubelka–Munk (K-M) function F(R) was obtained from the diffuse reflectance data R % using the following equation:

$$F(R) = \frac{(1-R)^2}{2R} \tag{2.5}$$

The Tauc's relation between the bandgap of a semiconductor and the optical absorption coefficient is given by the following equation:

$$(\alpha . h\nu) = A(h\nu - E_g)^n \tag{2.6}$$

where, A is a proportionality constant, α is the extinction coefficient, E_g is the bandgap of the semiconductor, n is an integer, ν is the frequency of incoming waves, and h is the Plank's constant. The integer n is calculated by the type of optical transitions and the typical values are $n = \frac{1}{2}$ and $n = 2$ for the direct and indirect band transition. Since the transformed K-M function F(R) is directly related to the extinction coefficient, the bandgap of the materials can be calculated using the following relation:

$$(F(R).h\nu) = A(h\nu - E_g)^n \quad (2.7)$$

2.4.7. UV-vis spectrophotometer

The optical absorption properties of the liquid samples were analyzed using a UV/Visible Scanning Spectrophotometer (Shimadzu UV-1900i). The absorption spectra provided insights into the material's optical activity, indicating whether it is responsive to visible or UV light. Beer-Lambert's Law states that absorbance is directly proportional to the concentration of the absorbing species and the path length of the medium through which light passes. It is given by

$$A = \varepsilon c l \quad (2.8)$$

where A is the absorbance, ε is the molar absorptivity (L mol^{-1} cm^{-1}), c is the concentration of the absorbing species (mol L^{-1}), l is the path length of the sample (cm). The path length l is fixed and corresponds to the width of the cuvette used to measure the solution's absorbance in the spectrophotometer as shown in Figure 2.14.

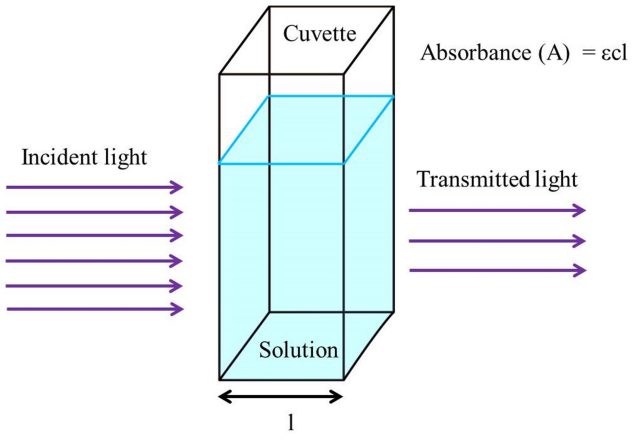

Figure 2.14. Illustration of Beer-Lambert's law.

The following characterizations were performed to determine the oxidation states and understand the vacancy states for obtaining the elemental composition of the photocatalytic materials:

2.4.8. X-ray photoelectron spectroscopy

The electronic states and chemical composition of the synthesized powder samples were analyzed using X-ray photoelectron spectroscopy (XPS) equipped with an Al Kα X-ray source (Thermo-125 Scientific, UK). The survey spectrum confirmed the presence of all constituent elements, while high-resolution spectra provided detailed insights into the oxidation states of the individual elements. The analysis was performed using XPS peak fitting software and literature references. The results helped validate the chemical formula of the material, complementing findings from other characterization techniques such as X-ray diffraction (XRD) and Raman spectroscopy.

2.4.9. Electron spin resonance spectrometer

The electron spin resonance (ESR) spectra were recorded using an electron spin resonance (ESR) spectrometer (JES-FA200, JEOL). ESR, also known as Electron Paramagnetic Resonance (EPR), provides critical insights into the electronic and magnetic properties of materials, particularly those containing unpaired electrons. It is highly sensitive to paramagnetic defects, such as oxygen vacancies in metal oxides, enabling the identification of their presence, concentration, and type based on unique g-values. Additionally, ESR can distinguish between different oxidation states of transition metal ions (e.g., Fe^{2+} vs. Fe^{3+} or Ti^{3+} vs. Ti^{4+}), offering valuable information on the electronic structure and redox behavior of the material.

2.4.10. Electrochemical experiment

Electrochemical experiments were performed using a CH Instruments Model 660E Series workstation. For Mott–Schottky (M–S) measurements, a thin film of the sample was prepared on the conductive surface of a glassy carbon electrode as follows: 80 mg of the powder sample was transferred to a clean, dry mortar. Then, 0.5 mL of polyvinyl alcohol (PVA, 0.01 g/mL) solution was added and ground with a pestle to form a paste. This step was repeated three additional times with successive 0.5 mL additions of PVA solution, with thorough grinding after each addition, to obtain a uniformly sticky paste.

A few drops of the resulting paste was applied to the electrode surface using a micropipette, ensuring no air bubbles were formed.

A three-electrode configuration was employed, consisting of a platinum wire as the counter electrode, a standard Ag/AgCl electrode (in 1 M KCl) as the reference, and the prepared glassy carbon electrode as the working electrode. M–S measurements were conducted in 0.1 M Na_2SO_4 electrolyte (pH 7) at a frequency of 1000 Hz using the impedance-potential (IMPE) technique.

2.5. Kinetics study

A photocatalytic reactor set-up with an operable door (shown in Figure 2.15) was developed to perform the dye degradation experiment. The photoactivity experiments were conducted in a controlled environment, ensuring that the observed results were solely attributed to the controlled light source and not influenced by any external light exposure.

2.5.1. Photocatalytic degradation kinetics

The photocatalytic degradation performance of the photocatalysts was evaluated using the degradation of dyes including methylene blue (MB), rhodamine B (RhB), and phenol under visible light irradiation **(**SANSI LED bulb, $\lambda > 400$ nm**)**. The spectrum of the light is shown in Figure 2.16. The intensity of visible irradiance was 46 mW/cm^2. A 0.01 mM MB/RhB and 0.05 mM phenol solution was prepared with a catalyst loading of 0.5 g/L. Prior to light irradiation, the catalyst-dye solution was stirred in the dark to achieve adsorption-desorption equilibrium. The suspension was then exposed to visible light, and aliquots were collected at 15-minute intervals. The degradation of MB was monitored by measuring the optical density of the solution using a Shimadzu 1900i spectrophotometer. The rate constants were calculated using the pseudo-first-order kinetics equation based on Langmuir–Hinshelwood model

$$kt = ln\, C/C_0 \tag{2.9}$$

where k is the rate constant, t is the time, C_0 is the initial concentration and C is the final concentration.

The reusability of the photocatalyst was evaluated under the same experimental setup and light source, for three/four consecutive cycles. At the start of each cycle, the

MB concentration was adjusted to its initial value (0 min of the 1st cycle) before initiating light irradiation. The decline in photocatalytic activity after the last cycle serves as an indicator of the photocatalyst's stability and robustness.

The photocatalytic degradation of organic pollutants relies on reactive species such as holes (h^+), electrons (e^-), superoxide radicals ($^{\bullet}O_2^-$), hydroxyl radicals ($^{\bullet}OH$), and singlet oxygen ($^1O_2$). To investigate the role of these active species in the photocatalysis process, quenching agents were used: ammonium oxalate (AO) for h^+, silver nitrate (SN) for e^-, p-benzoquinone (BQ) for $^{\bullet}O_2^-$, isopropyl alcohol (IPA) for $^{\bullet}OH$, and L-histidine (LH) for $^1O_2$. The MB concentration, catalyst loading, and evaluation process were maintained consistent with those used in the photocatalytic degradation experiments.

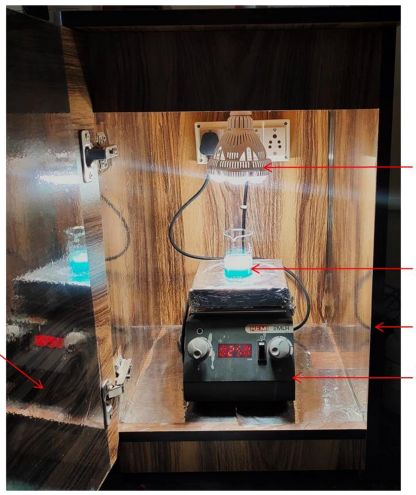

Figure 2.15. Inside view of reactor set-up.

UV(380-399nm)	Blue (400-499nm)	Green (500-599nm)	Red (600-699nm)	FR (700-780nm)
0.05%	19.41%	37.7%	36.23%	6.61%

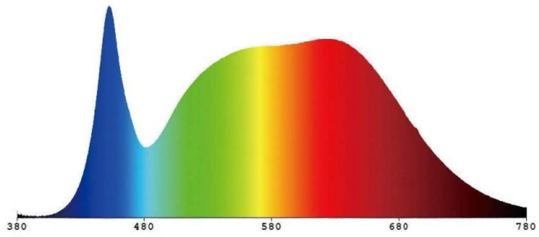

Figure 2.16. Energy spectrum (Intensity vs wavelength) of SANSI LED bulb.